IOP Publishing Plasma Sources Science and Technology
Plasma Sources Sci. Technol. **29** (2020) 075001 (7pp) https://doi.org/10.1088/1361-6595/ab9b19

Computational study of plasma-induced flow instabilities in power modulated atmospheric-pressure microwave plasma jet

M Kubečka[1], M Snirer, A Obrusník, V Kudrle and Z Bonaventura

Department of Physical Electronics at the Faculty of Science, Masaryk University, Brno, Czech Republic

E-mail: kubecka@mail.muni.cz, snirer@mail.muni.cz, adamobrusnik@physics.muni.cz and zbona@physics.muni.cz

Received 1 October 2019, revised 5 May 2020
Accepted for publication 9 June 2020
Published 9 July 2020

Abstract

This work presents a combined experimental and simulation-based investigation of gas flow perturbations caused by atmospheric-pressure microwave plasma jet with modulated power. These plasma-induced flow instabilities are observed experimentally by schlieren imaging and the mechanism of their formation is explained using a numerical model. The model offers a time-resolved self-consistent solution of plasma dynamics, gas flow, and heat transfer equations. The simulation results are in good agreement with the experimental observations and we conclude that the key mechanism behind the flow perturbations is rapid gas heating at the end of the discharge tube.

Keywords: numerical simulation, microwave plasma, flow instability, plasma jet

(Some figures may appear in colour only in the online journal)

1. Introduction

Microwave induced plasma (MIP) is a subject of interest mainly due to its ability to produce large densities of reactive species and for the high efficiency of energy transfer between the electromagnetic wave and the plasma. Although atmospheric-pressure MIPs were conventionally thought of as high power plasma sources, recent research has also extended their applicability into the low-power/low gas temperature regime [1]. Thanks to this flexibility, MIPs are widely used in many industrial application such as synthesis of graphene [2], biomedical applications [3], surface treatment [4], pollutant degradation [5] or gas reforming [6]. In some of these applications, the microwave power is not delivered continuously but is modulated with Hz–kHz frequencies [7].

In earlier works, it was experimentally demonstrated that power modulation of MIP produces flow perturbations which enhance the gas mixing in the active plasma zone [8]. These flow perturbations are potentially very important for the applications of MIP because they enhance species and energy transport. The topic of flow instabilities has recently been receiving considerable attention in the field of dielectric-barrier discharges (DBD), where it was investigated both theoretically [9] and experimentally [10]. The gas dynamics perturbations in MIP were studied several times with the focus on the shock wave phenomena occurring during the discharge initiation [11], on the UV emission of filamentary structures [12], the experimental observation of the argon and helium microplasma behaviour [13] or with the focus on the energy distribution function in the ionization waves [14].

In this work, we aim to explain the origin of flow-induced instabilities in a power modulated MIP using a numerical model. The presented model is innovative in the sense that it self-consistently solves the coupled system of plasma transport equations, gas dynamics equations and the heat equation

[1] Author to whom any correspondence should be addressed.

and solves them in time. This allows one to investigate the time-dependent power modulations, which has not been possible in similar models focused on the steady state solution [15–17]. The model is compared with schlieren imaging, observing that the imaged density gradients show similar structures as the simulation temperature gradients. Unlike the recently published work [10] and the earlier works [18, 19], which all concluded that the flow instabilities in DBDs are caused by the EHD force, we conclude that the onset of flow instabilities in MIPs can be explained by rapid gas heating only.

2. Numerical model

The model described in this section is a fully coupled 2D axially-symmetrical one and was partially derived from earlier work of Baeva *et al* [15] where the mass and energy transport equations for electrons in the drift-diffusion form, the drift-diffusion transport equation for ions and diffusion equation for excited metastable atoms are solved. These equations are coupled to compressible Navier–Stokes equations and heat transfer for the background gas. The self-consistent equations are also time dependent since we are interested in the formation and propagation of the flow perturbations.

2.1. Model assumptions

The model consists of several assumptions listed below

(a) The model is based on continuum approximation for fluids.
(b) Heavy particles and electrons have different temperature. Heavy particles are in thermal equilibrium.
(c) Electrons are described by the Maxwellian energy distribution.
(d) The plasma chemistry consists solely electrons, ground-state and metastable argon atoms and atomic and molecular argon ions. These species undergo 17 volume reactions and 4 surface reactions.
(e) The fluid flow is assumed to be laminar and compressible. The assumption of laminar flow is not true in the downstream region, where the rapidly cooling and decelerating gas was observed to trigger eddies. However the reasonable agreement of model and experiment shows that the phenomena described in the vicinity of the discharge tube end do not require turbulence model. The influence of the temperature gradients was included via flow compressibility and diagonality of the viscous stress tensor.

2.2. Equations solved

The self-consistent fluid model of microwave plasma solve the electromagnetic field, transport equations for plasma species, heat transfer and Navier–Stokes equations. The microwave electromagnetic field is computed from the wave equation in the form

$$\nabla \times \mu_{\mathrm{r}}^{-1} (\nabla \times \mathbf{E}) - k_0^2 \left(\varepsilon_{\mathrm{r}} - j \frac{\sigma}{\varepsilon_0 \omega} \right) \mathbf{E}, \tag{1}$$

where $\mathbf{E}$ is the electric field, ε_{r} and μ_{r} are relative permittivity and relative permeability, respectively, k_0 is the free-space wave number, ε_0 is a permittivity of the vacuum, ω is the angular field frequency and σ is the electric conductivity. The electrostatic field is solved with Poisson's equation

$$\nabla \cdot (\varepsilon_{\mathrm{r}} \nabla \phi) = -\frac{\rho}{\varepsilon_0}, \tag{2}$$

where ϕ is the electric potential and ρ is the space charge density which is generally computed as

$$\rho = q \left(\sum_{k=1}^{Q} Z_k n_k - n_{\mathrm{e}} \right), \tag{3}$$

where the index $k = 1, \ldots, Q$ runs over ions (Ar^+ and Ar_2^+), q is the elementary charge, Z_k is the charge of kth species, and n_k and n_{e} are kth species density and electron density, respectively.

The electron density and energy balance are described by the following two transport equations in the drift-diffusion form

$$\frac{\partial}{\partial t} n_{\mathrm{e}} + \nabla \cdot \mathbf{\Gamma}_{\mathrm{e}} = R_{\mathrm{e}}, \tag{4}$$

$$\frac{\partial}{\partial t} n_{\varepsilon} + \nabla \cdot \mathbf{\Gamma}_{\varepsilon} + \mathbf{E} \cdot \mathbf{\Gamma}_{\mathrm{e}} = S_{\mathrm{en}} - (\mathbf{u} \cdot \nabla) n_{\varepsilon} + \frac{\mathbf{Q}}{q}, \tag{5}$$

where $\mathbf{\Gamma}_{\mathrm{e}}$ is the electron flux vector and R_{e} is either a source or a sink of electrons. In similar matter the $\mathbf{\Gamma}_{\varepsilon}$ describe the electron energy flux vector, n_{ε} is the electron energy density, S_{en} describe either gain or loss of the electron energy and $\mathbf{Q}$ is the heat source. The electron flux vector $\mathbf{\Gamma}_{\mathrm{e}}$ is defined as

$$\mathbf{\Gamma}_{\mathrm{e}} = -(\mu_{\mathrm{e}} \mathbf{E}) n_{\mathrm{e}} - \nabla (D_{\mathrm{e}} n_{\mathrm{e}}) + \mathbf{u} n_{\mathrm{e}}. \tag{6}$$

The first term on the right side describe the drift of electrons, where the μ_{e} is the electron mobility. The second term describe diffusion of electrons, where D_{e} is the electron diffusion. The last term describe a convection where $\mathbf{u}$ is the mean velocity of the fluid. The electron diffusion and the electron mobility are defined as

$$\mu_{\mathrm{e}} = \frac{q}{m_{\mathrm{e}} \nu_{\mathrm{m}}}, \quad D_{\mathrm{e}} = \frac{k_{\mathrm{B}} T_{\mathrm{e}}}{m_{\mathrm{e}} \nu_{\mathrm{m}}}, \tag{7}$$

where ν_{m} is the momentum transfer frequency, T_{e} is the electron temperature and m_{e} is the electron mass. The momentum transfer frequency for the a given mean energy is calculated directly from the cross-sections. The source term R_{e} is describe as

$$R_{\mathrm{e}} = \sum_{j=1}^{M} x_j k_j N_n n_{\mathrm{e}}, \tag{8}$$

where x_j is the mole fraction of the target species for reaction j, k_j denotes the rate coefficient for reaction j and the N_n is the total number density of neutral species. The rate coefficients are shown in table 1 at the end of the document. The electron energy gain or loss is defined in a similar way with additional term $\Delta\varepsilon_j$ describing the energy loss from reaction j

$$S_{\mathrm{en}} = \sum_{j=1}^{P} x_j k_j N_n n_{\mathrm{e}} \Delta\varepsilon_j. \tag{9}$$

The expressions for R_e and S_{en} above are formulated for two-body reactions, expressions for three-body reactions are formulated analogically. The heat source $\mathbf{Q}$ for electrons describe the absorbed microwave power and is defined as

$$\mathbf{Q} = \frac{1}{2}\Re\left(\boldsymbol{J}\cdot\boldsymbol{E}^{*}\right), \tag{10}$$

where $\boldsymbol{J}$ is the total current density. The electron energy flux is defined in a similar way as the electron flux as

$$\boldsymbol{\Gamma}_{\varepsilon} = -(\mu_{\varepsilon}\mathbf{E})n_{\varepsilon} - \nabla(D_{\varepsilon}n_{\varepsilon}) + \mathbf{u}n_{\varepsilon}, \tag{11}$$

where μ_{ε} is the electron energy mobility, the electron energy diffusivity D_{ε} is linked with electron diffusivity as $D_{\varepsilon} = \frac{5}{3}D_e$. The electron energy density n_{ε} and the mean electron energy $\bar{\varepsilon}$ are defined as

$$\bar{\varepsilon} = \frac{n_{\varepsilon}}{n_e}, \quad \text{where } n_{\varepsilon} = \frac{3}{2}n_e T_e. \tag{12}$$

The heavy species are solved by the transport equation defined as

$$\rho\frac{\partial}{\partial t}(w_k) + \rho(\mathbf{u}\cdot\nabla)w_k = \nabla\cdot\mathbf{j}_k + R_k, \tag{13}$$

where w_k is the mass fraction of kth species, $\mathbf{j}_k$ is the diffusive flux vector, R_k describe the production or loss of the corresponding species k, $\mathbf{u}$ is the mass averaged fluid velocity vector and ρ is the mixture density. The species reactions are listed in table 2. The diffusive flux vector is defined as

$$\mathbf{j}_k = \rho w_k \mathbf{V}_k, \tag{14}$$

where the $\mathbf{V}_k$ is the multicomponent diffusion velocity for kth species. Using the mixture-average approximation, the multicomponent diffusion velocity could be defined as

$$\mathbf{V}_k = D_{k,\mathrm{m}}\frac{\nabla w_k}{w_k} + D_{k,\mathrm{m}}\frac{\nabla M_n}{M_n} - z_k\mu_{k,\mathrm{m}}\mathbf{E}, \tag{15}$$

the $D_{k,\mathrm{m}}$ is the mixture averaged diffusion coefficient, M_n is the mean molar mass of the mixture, z_k is the charge number of species k, $\mu_{k,\mathrm{m}}$ is the mixture averaged mobility for species k. The diffusion coefficient $D_{k,\mathrm{m}}$ is than defined as

$$D_{k,\mathrm{m}} = \frac{1 - w_k}{\sum_{j\neq k}^{Q} x_j/D_{kj}}. \tag{16}$$

The diffusion coefficients D_{kj} can be found in [20]. The mean molar mass M_n and the mole fraction x_k for species k is defined as

$$\frac{1}{M_n} = \sum_{k=1}^{Q}\frac{w_k}{M_k}, \quad x_k = \frac{w_k}{M_k}M_n. \tag{17}$$

The mixture averaged mobility for species k is defined as

$$\mu_{k,\,\mathrm{m}} = \frac{qD_{k,\,\mathrm{m}}}{k_B T}. \tag{18}$$

The mixture density ρ is define by the ideal gas law as

$$\rho = \frac{pM_n}{RT}, \tag{19}$$

Table 1. Table of boundary conditions used in model.

Boundary conditions	Boundary section
Axial symmetry	aq
GAS DYNAMICS	
Inlet	ab
Outlet	opq
Wall	bsrno
HEAT TRANSFER	
Temperature	abcdtl
Outflow	klopq
PLASMA AND ELECTRIC FIELD	
Microwave port	fg
Wall	bsrno
Ground	bsrno
Scattering boundary conditions	ab, klopq
Dielectric contact	bsrno
Insulation	ab, opq
Zero charge	ab, opq
Perfect electric conductor	cdef, ghijk

where R is the universal gas constant. The term R_k describing the production or loss of the kth species is defined as

$$R_k = M_n\sum_{j=1}^{N}\nu_{kj}r_j. \tag{20}$$

The heat transfer is described by following equation

$$\rho C_p\frac{\partial T}{\partial t} + \rho C_p\mathbf{u}\cdot\nabla T - (\nabla\cdot\kappa\nabla T) = \mathbf{Q}_{\mathrm{gas}}, \tag{21}$$

where C_p is the specific heat capacity, ρ is the density of the gas, T is the gas temperature, κ is the thermal conductivity and $\mathbf{Q}_{\mathrm{gas}}$ the heat source accounting for the energy exchange between electrons and heavy particles. In this model, the exchange is mediated only by elastic collisions.

The fluid flow is described by compressible Navier–Stokes equations even that the Mach number is smaller than 1. This is purposefully chosen since the gradients in gas density are non-negligible. The flow is assumed to be laminar and also the viscous tensor does not include any turbulent terms. The continuity equation and the momentum equations are defined as follows (respectively)

$$\frac{\partial\rho}{\partial t} + \nabla\cdot(\rho\,\mathbf{u}) = 0, \tag{22}$$

$$\rho\frac{\partial\mathbf{u}}{\partial t} + \rho(\mathbf{u}\cdot\nabla)\mathbf{u} = \nabla\cdot[-p\mathbf{I} + \boldsymbol{\tau}], \tag{23}$$

here $\mathbf{u}$ is the velocity vector, p is pressure, $\mathbf{I}$ is the identity tensor and $\boldsymbol{\tau}$ is the viscous stress tensor. The viscous stress tensor $\boldsymbol{\tau}$ is defined as

$$\boldsymbol{\tau} = \eta(\nabla\mathbf{u} + (\nabla\mathbf{u})^T) - \frac{2}{3}\eta(\nabla\cdot\mathbf{u})\mathbf{I}, \tag{24}$$

where the η represents the dynamic viscosity.

Table 2. Set of kinetic reactions included in the fluid model.[a,b] The excited argon atoms Ar^* includes both the Ar(4s) and Ar(4p) state.

VOLUME REACTIONS

j	Process	Rate coefficient		$\Delta\varepsilon$(eV)	Reference
1	$e + Ar \rightarrow e + Ar$	BOLSIG+		0	[22]
2	$e + Ar \rightarrow e + Ar^*$	BOLSIG+		11.5	[22]
3	$e + Ar^* \rightarrow e + Ar$	BOLSIG+		−11.5	[22]
4	$e + Ar \rightarrow 2e + Ar^+$	BOLSIG+		15.8	[22]
5	$e + Ar^* \rightarrow 2e + Ar^+$	BOLSIG+		4.24	[22]
6	$e + Ar_2^* \rightarrow 2e + Ar_2^+$	$k_6 = 5.4 \times 10^{10} \times T_e^{0.7}$	$m^3\ (s^{-1}\ mol)^{-1}$	3.55	[21]
7	$e + Ar_2^* \rightarrow e + 2Ar$	$k_7 = 6.022 \times 10^{11}$	$m^3\ (s^{-1}\ mol^{-1})^{-1}$	−10.95	[21]
8	$e + Ar_2^+ \rightarrow Ar^* + Ar$	$k_8 = 6.263 \times 10^{11} \times \left(\frac{0.026}{T_e}\right)^{0.67} \times \left(\frac{1-\exp(-418/T)}{1-0.31\times\exp(-418/T)}\right)$	$m^3\ (s^{-1}\ mol^{-1})^{-1}$	−3	[23]
9	$e + Ar_2^+ \rightarrow e + Ar + Ar^+$	$k_9 = 6.685 \times 10^{11} \times \exp\left(\left(-2.94 + 3\left(\frac{T}{11600} - 0.026\right)\right)/T_e\right)$	$m^3\ (s^{-1}\ mol^{-1})^{-1}$	1.26	[23]
10	$Ar^* + Ar^* \rightarrow e + Ar + Ar^+$	$k_{10} = 9.785 \times 10^7 \times T^{0.5}$	$m^3\ (s^{-1}\ mol)^{-1}$	—	[23]
11	$Ar^* + Ar \rightarrow Ar + Ar$	$k_{11} = 1807$	$m^3\ (s^{-1}\ mol^{-1})^{-1}$	—	[21]
12	$Ar_2^* + Ar_2^* \rightarrow 2Ar + e + Ar_2^+$	$k_{12} = 9.785 \times 10^7 \times T^{0.5}$	$m^3\ (s^{-1}\ mol^{-1})^{-1}$	—	[23]
13	$2Ar + Ar^+ \rightarrow Ar + Ar_2^+$	$k_{13} = 2.72 \times 10^7 \times T^{-1}$	$m^6\ (s^{-1}\ mol^{-2})^{-1}$	—	[23]
14	$2Ar + Ar^* \rightarrow Ar_2^* + Ar$	$k_{14} = 1.197 \times 10^4$	$m^6\ (s^{-1}\ mol^{-2})^{-1}$	—	[23]
15	$Ar + Ar_2^+ \rightarrow 2Ar + Ar^+$	$k_{15} = 3.649 \times 10^{12} \times T^{-1}\ \exp\left(-\frac{1.238\times10^5}{RT}\right)$	$m^3\ (s^{-1}\ mol^{-1})^{-1}$	—	[23]
16	$Ar^* \rightarrow Ar$	$k_{16} = 3.145 \times 10^5$	s^{-1}	—	[23]
17	$Ar_2^* \rightarrow Ar + Ar$	$k_{17} = 6 \times 10^7$	s^{-1}	—	[23]

SURFACE REACTIONS

	Sticking coefficient	Reference
$Ar^* \rightarrow Ar$	$\gamma = 1$	—
$Ar_2^* \rightarrow 2Ar$	$\gamma = 1$	—
$Ar^+ \rightarrow Ar$	$\gamma = 1$	—
$Ar_2^+ \rightarrow 2Ar$	$\gamma = 1$	—

[a]Electron temperature T_e in the rate coefficients is given in [K] as well as the temperature of the neutral gas T.
[b]For the empirical measured rate coefficients k_j the temperature is dimensionless unit.

2.3. Domain and boundary conditions

The computational domain is shown in the figure 1. It is composed of a silica discharge tube [bcdtrs], Teflon ring [mnrt], plexiglass plateau [lmno] and resonator cavity [defghijk]. Cylindrically symmetric 2D geometry is discretized using an unstructured triangular grid where the element surface is varying between 6.3×10^{-6} m^2 and 6.4×10^{-10} m^2.

The geometry contains several boundaries listed in table 1. For the gas dynamics we impose for the *inlet* the Dirichlet boundary condition where we set the net flux into the domain. At the *outlet* we impose the Neumann boundary condition (zero derivative). At the *wall* the gas velocity was set to zero. For the heat transfer boundary conditions we set the *temperature* on the wall and inlet at 300 K. At the *outflow* the temperature gradient in the normal direction is zero. This means that most of the heat is transported away from the computational domain by convection. The electromagnetic energy enters the domain via coaxial *microwave port* with frequency of 2.45 GHz. The *wall* boundary condition ensures the loss of electrons due to a net flux of electrons from the plasma bulk and due to random motion of electrons within the mean free path. The *ground* sets boundaries to a zero potential. The *scattering boundary condition* make a boundary transparent for a scattered wave and incoming plane wave. The *dielectric contact* compute the surface charge accumulations due to the interaction between plasma and dielectric surface. The *insulation* sets the normal component of the electron flux and electron energy flux to zero. The *zero charge* sets the charge on

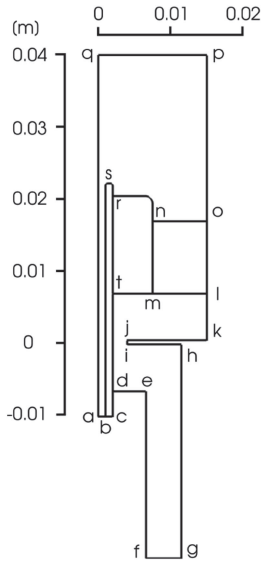

Figure 1. Geometry of the modeled domain.

the boundary to zero. The *perfect electric conductor* sets the tangential component of the electric field to zero [21].

2.4. Numerical method

The model is implemented using COMSOL Multiphysics (version 5.2) [21] based on the finite element method (FEM). To obtain the solution of our highly non-linear model, we had to use the multi-step process consisting of

(a) Solving the laminar flow.
(b) Solving the plasma module with pre-computed velocity field at background (for lower values of pressure due to the model stability).
(c) Coupling the plasma module with heat transfer and fluid flow.
(d) Ramping the pressure to the target conditions.
(e) Solving with the power modulation.

To prevent memory effect from '(4) pressure ramp step', we run several (typically 5) power modulation periods until the solution does not change between periods.

3. Experimental and model set-up

For investigation of the plasma-induced flow instabilities, we chose a surface-wave-sustained discharge (SWDs) generated by a surfatron [24]. The experimental setup consists of a resonator (SAIREM Surfatron 80) placed around a silica tube with 2 mm inner diameter and 4 mm outer diameter. A plexiglass plate is placed 20 mm above the launching gap to avoid any interference of the cooling air escaping from the resonator thorough the launching gap. The model faithfully reproduces the experimental geometry, see figure 1.

The silica tube is connected to a mass flow controller (Omega FMA5400/5500) that supplies 365 sccm of argon through the quartz tube. The microwave power with frequency of 2.45 GHz is fed though a coaxial cable from a microwave generator (SAIREM GMP 20 KED) and time-modulated (Keysight Agilent 33 500) by a $f_{\mathrm{mod}} = 1$ kHz sine wave. In experiment, the mean generator power is 240 W with $\pm$75 W amplitude. Based on earlier measurements, it was estimated that approximately 40% of the input power is coupled to the plasma, so the mean power in the model was set to 100 W with the amplitude of 31.25 W. In other words, the absorbed plasma power is given as

$$P(t) = 100\,[\mathrm{W}] + 31.25\,[\mathrm{W}] \cdot \sin\left(2\pi \cdot f_{\mathrm{mod}}\,[\mathrm{Hz}] \cdot t\right). \quad (25)$$

We also decided to simulate an argon plasma jet ejected into argon atmosphere, rather than ambient air. By this choice, we illustrate that air chemistry is not needed for the onset of the instability and that the mechanism of formation can be purely thermal in MIPs.

The experimental measurement consists of time-resolved schlieren photography. A schematic diagram of the experimental setup is shown in figure 2. The Z-type schlieren system consists of two spherical aluminized first surface mirrors (f/10, 150 mm diameter, λ/8), 20 W Luminus LED light source, razor edge and an ICCD camera (Princeton Instruments PI-MAX 3, 105 mm Sigma lens, Soligor C/D7 2x teleconverter) with gate width of 5 μm, 40 gain, resolution of 1 Mpx and 100 accumulations. Time resolution was much smaller than the power modulation pulse frequency in order to capture the propagation of the plasma-induced flow instabilities.

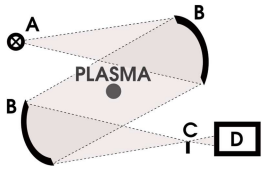

Figure 2. A schematic of the Z-type two-mirror schlieren system consists of LED light source (A), two spherical mirrors (B), razor edge (C) an ICCD camera (D).

4. Results and discussions

To understand the mechanism behind the flow instabilities, we first have to validate that the computer simulation reproduced the experimentally observed flow instabilities. Figures 3(a)–(d) compare the experimentally obtained results by schlieren photography and the simulation results for the same times within one period of the power modulation. Apparently, the simulated propagation velocity, the shape and the size of the flow instability are in good agreement with the experiment. This suggests that the model captures all the physics necessary for explaining the origin of the flow instability. At the beginning of the period, as the input power rises, the flow perturbation begins to form within the first 100 μs of the 1000 μs period as shown in the figure 3(a). This perturbation grows at the tip of plasma jet plume and it moves in the direction of the feed gas flow.

Shortly after reaching the power maximum, the front of the flow perturbation is formed. The newly established shear flow around the instability edges enhances the gas mixing between the feed gas and the background atmosphere as is shown in figure 3(b) (left) and reported in [8]. If the argon jet was ejected into ambient air, this would enhance the transport of different ambient species into the active plasma plume. With argon plasma in argon atmosphere, the instability only enhances energy transfer. Both the simulation and the experiment show, that the flow instability propagates with the velocity of the gas flow. In the middle of the period, the flow perturbation is fully developed as shown in figure 3(c) and is launched away from the plasma plume.

Figure 3(d) shows the detachment of the flow perturbation from the plasma plume. After the power decreases there is a pressure drop inside the discharge tube resulting in backflow of ambient gas into the discharge tube as is shown in figure 3(d) (left). This is consistent with previous experimental observations by Voráč *et al* [8].

The slight differences between the experimental and simulated results in figures 3(a)–(d) can be attributed to one or both of the following facts:

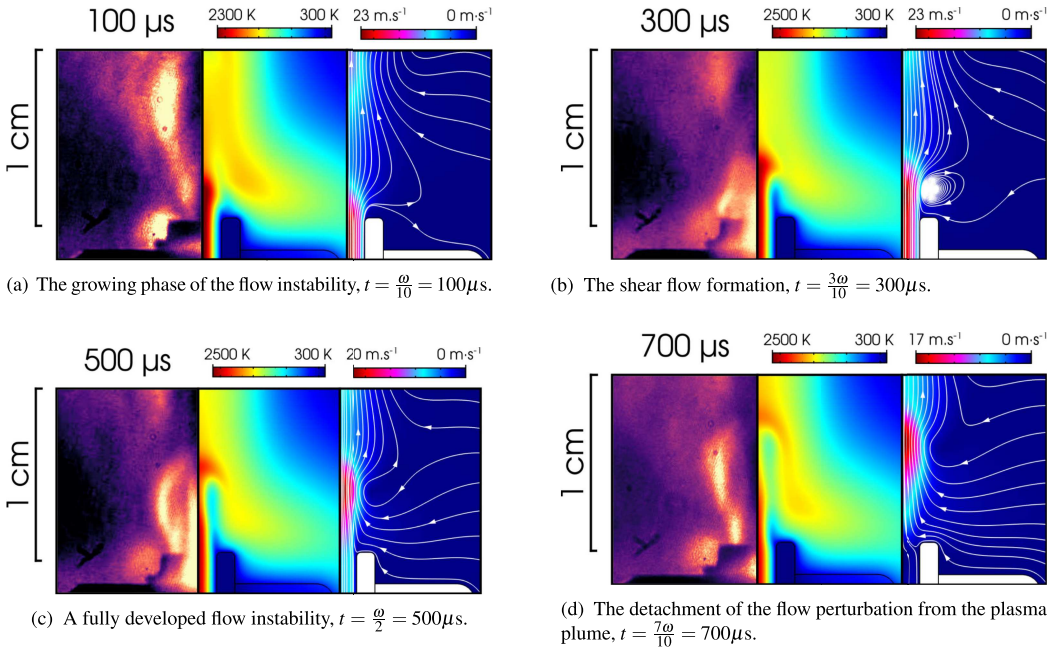

(a) The growing phase of the flow instability, $t = \frac{\omega}{10} = 100\mu$s.

(b) The shear flow formation, $t = \frac{3\omega}{10} = 300\mu$s.

(c) A fully developed flow instability, $t = \frac{\omega}{2} = 500\mu$s.

(d) The detachment of the flow perturbation from the plasma plume, $t = \frac{7\omega}{10} = 700\mu$s.

Figure 3. Schlieren image (plotted with false colors) averaged over 100 periods of the discharge power modulation (left), the simulated gas temperature (middle) and the calculated surface velocity magnitude with the velocity field streamlines (left) at various times during the modulation period.

(a) The experimental results are temporally averaged over 100 periods of the power modulation. The random oscillations could blur the result schlieren image.

(b) In the experimental setup the feed gas (argon) emerges into an ambient air, while in the simulation the whole domain contains solely an argon. As a consequence, the temperature drop in the simulation could be underestimated.

Figure 4 provides basic insight into the plasma dynamics leading to the formation of the flow instability:

(a) As the microwave power increases during $\langle 0, \pi/2 \rangle$, it is instantaneously absorbed by electrons. The electron heating term, denoted Q_{rh}, reaches maximum exactly at $\frac{\pi}{2}$.

(b) As the electron temperature increases, so does the elastic transfer of energy from electrons to the background gas. The gas heating term Q_{gas} reaches maximum a few μs after the plasma power peaks.

(c) Finally, the gas temperature T reaches maximum approximately 20 μs after the plasma power peaks and then starts decreasing, as the instability is carried away with the gas flow.

To look at the instability formation in more detail, we provide axially-resolved plots of Q_{rh}, Q_{gas} and T in figure 5. We immediately see that the power absorption occurs primarily in the resonator cavity (see figure 5(a)). This is characteristic for surface-wave sustained discharges and it is caused by the fact that the plasma acts as a lossy conductor for microwaves. However, a second peak of the power absorption occurs in the proximity of the end of the discharge tube and is quite noticeable during the power modulation period. Interestingly,

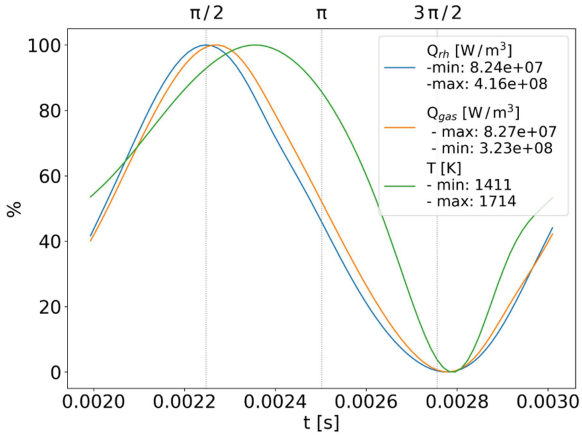

Figure 4. The time evolution of the electron heating term Q_{rh}, the gas heating term Q_{gas} and the gas temperature T at the end of the discharge tube ($r = 0$ mm, $z = 2.25$ mm).

the power absorption peak inside the resonator changes only slightly during the modulation period (by approx. 25%) while the second power absorption peak at the end of the discharge tube varies by over a factor of 2. Figure 5(c) also shows that the temperature within the quartz tube remains fairly stable throughout the power modulation period and it is only the temperature outside the tube, that varies approximately by ± 400 K ($\pm 25\%$ with respect to the mean temperature). It is important to point out that as the plasma power reaches the minimum value at $\frac{3\pi}{2}$, the gas temperature inside the tube does not decrease much, but the temperature immediately in front of the tube does. This is due to the fact that the cold surrounding gas is being sucked into the region immediately outside the discharge tube. This evidence strongly suggests that the flow

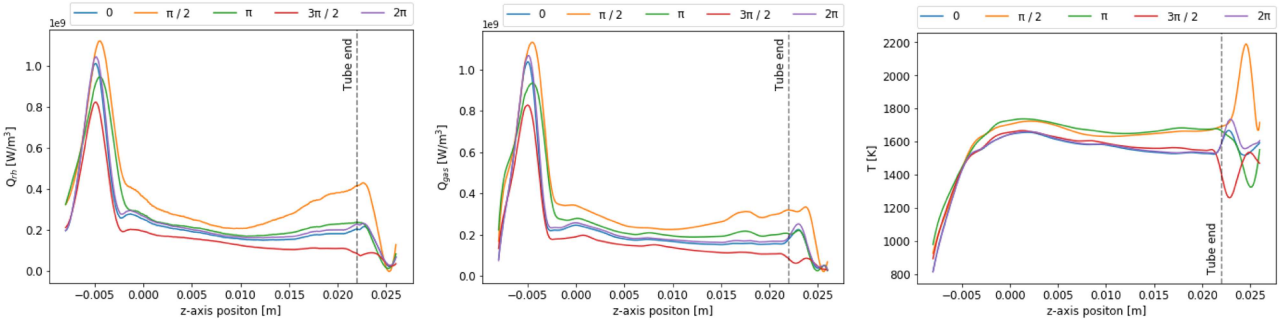

Figure 5. Axial plots of the electron heating term Q_{rh}, gas heating term Q_{gas} and gas temperature T at $r = 0.5$ mm. The microwave launching gap is located at $z = 0$ mm.

instabilities are triggered by the variations in power absorption at the end of the discharge tube.

The discussion above clearly illustrates that gas flow instabilities in power-modulated MIPs lead to enhanced transport of ambient gas into the plasma plume. In the presented model, this transport is only manifested as a temperature drop just outside the plasma jet orifice. However, if the jet was emerged into ambient air, the flow instability would cause enhanced transport of N_2, O_2 and H_2O molecules into the plasma plume. Thereby, the fluence of reactive species produced by the plasma would be increased, as opposed to the case of constant power.

5. Conclusion

By investigating the power transfer mechanisms in the numerical model, we were also able to identify the precise mechanism of formation of the flow instabilities. It was shown that the instabilities originate primarily at the end of the discharge tube, where most of the microwave power is absorbed by electrons. It should also be highlighted that by excluding the ambient air from the simulation, we proved that the formation of a downstream instability in atmospheric-pressure MIPs is not conditioned by argon–air plasma chemistry and its onset can be purely thermal. The rate, at which the instability is formed is certainly influenced by the amplitude of power modulation and the waveform, which is what we intend to investigate in follow-up work.

Acknowledgments

This research was supported by project LM2018097 funded by the Ministry of Education, Youth and Sports of the Czech Republic.

ORCID iDs

M Kubečka https://orcid.org/0000-0002-9874-5718
M Snirer https://orcid.org/0000-0003-0534-5262
Z Bonaventura https://orcid.org/0000-0002-9591-6040

References

[1] Fu W, Zhang C, Nie C, Li X and Yan Y 2019 *Appl. Phys. Lett.* **114** 254106
[2] Tatarova E, Henriques J, Luhrs C, Dias A, Phillips J, Abrashev M and Ferreira C 2013 *Appl. Phys. Lett.* **103** 134101
[3] Benova E, Atanasova M, Bogdanov T, Marinova P, Krcma F, Mazankova V and Dostal L 2016 *Plasma Med.* **6** 59–65
[4] Hnilica J, Kudrle V and Potocnakova L 2012 *IEEE Trans. Plasma Sci.* **40** 2925–30
[5] Kim H H 2004 *Plasma Processes Polym.* **1** 91–110
[6] Yanguas-Gil A, Hueso J L, Cotrino J, Caballero A and González-Elipe A R 2004 *Appl. Phys. Lett.* **85** 4004–6
[7] Hnilica J, Schäfer J, Foest R, Zajíčková L and Kudrle V 2013 *J. Phys. D: Appl. Phys.* **46** 335202
[8] Voráč J, Potočňáková L, Synek P, Hnilica J and Kudrle V 2016 *Plasma Sources Sci. Technol.* **25** 025018
[9] Lietz A M, Johnsen E and Kushner M J 2017 *Appl. Phys. Lett.* **111** 114101
[10] Tang Y, Yao Q, Cui W, Pu Y and Li S 2018 *Appl. Phys. Lett.* **113** 224101
[11] Aleksandrov A F, Shibkov V M and Shibkova L V 2010 *High Temp.* **48** 611–9
[12] Vikharev A, Gorbachev A, Ivanov A and Kolysko A 1994 *Zh. Eksp. Teor. Fiz.* **106** 172–85
[13] Hoskinson A R, Yared A and Hopwood J 2015 *Plasma Sources Sci. Technol.* **24** 055002
[14] Kozakov R, Wilke C, Golubovski Y B and Nekutchaev V 2004 *Czech. J. Phys.* **54** C630
[15] Baeva M, Bösel A, Ehlbeck J and Loffhagen D 2012 *Phys. Rev.* E **85** 056404
[16] Georgieva V *et al* 2017 *Plasma Process. Polym.* **14** 1600185
[17] Jimenez-Diaz M, Carbone E, van Dijk J and Van der Mullen J 2012 *J. Phys. D: Appl. Phys.* **45** 335204
[18] Robert E, Sarron V, Darny T, Riès D, Dozias S, Fontane J, Joly L and Pouvesle J M 2014 *Plasma Sources Sci. Technol.* **23** 012003
[19] Papadopoulos P K, Vafeas P, Svarnas P, Gazeli K, Hatzikonstantinou P M, Gkelios A and Clément F 2014 *J. Phys. D: Appl. Phys.* **47** 425203
[20] Cussler E L and Cussler E L 2009 *Diffusion: Mass Transfer in Fluid Systems* (Cambridge: Cambridge University Press)
[21] COMSOL Multiphysics® v. 5.2. www.comsol.com. COMSOL AB, Stockholm, Sweden (accessed: 2015)
[22] Hagelaar G and Pitchford L 2005 *Plasma Sources Sci. Technol.* **14** 722
[23] Hoskinson A R, Gregório J, Parsons S and Hopwood J 2015 *J. Appl. Phys.* **117** 163301
[24] Moisan M, Zakrzewski Z and Pantel R 1979 *J. Phys. D: Appl. Phys.* **12** 219